ACS OMEGA

Open Access

http://pubs.acs.org/journal/acsodf

Article

Iron Nanoparticle-Incorporated Laser-Induced Graphene Filters for Environmental Remediation via an *In Situ* Electro-Fenton Process

Najmul Haque Barbhuiya, Akhila M. Nair, Nandini Dixit, and Swatantra P. Singh*

Cite This: *ACS Omega* 2024, 9, 22819−22830

Read Online

ACCESS | Metrics & More | Article Recommendations | Supporting Information

ABSTRACT: Laser-induced graphene (LIG) has garnered much attention due to its facile and chemically free fabrication technique. Metal nanoparticle incorporation into the LIG matrix can improve its electrical and catalytical properties for environmental application. Here, we demonstrate the fabrication of nanoscale zerovalent iron (nZVI) nanoparticle-incorporated LIG (Fe-LIG) and sulfidized-nanoscale zerovalent iron (S-nZVI) nanoparticle-incorporated LIG (SFe-LIG) surfaces. The sheets were first fabricated to investigate nanoparticle loading, successful incorporation in the LIG matrix, and electrochemical performance as electrodes. Fe-LIG and SFe-LIG sheets showed ∼3−3.5 times more charge density as compared with the control LIG sheet. The XPS and its deconvolution confirmed the presence of nZVI and S-nZVI in the Fe-LIG and SFe-LIG surfaces, which can generate *in situ* hydroxyl radical (•OH) via iron activation of electrogenerated hydrogen peroxide (H_2O_2) in short *in situ* electro-Fenton process. After confirmation of the successful incorporation of iron-based nanoparticles in the LIG matrix, filters were fabricated to demonstrate the application in the flow-through filtration. The Fe-LIG and SFe-LIG filters showed ∼10−30% enhanced methylene blue removal under the application of 2.5 V at ∼1000 LMH flux. The Fe-LIG and SFe-LIG filters also showed complete 6-log bacteria and virus removal at 2.5 and 5 V, respectively, while the LIG filters showed only ∼4-log removal. Such enhanced removal by the Fe-LIG and SFe-LIG filters as compared to LIG filters is attributed to the improved charge density, electrochemical activity, and *in situ* electro-Fenton process. The study shows the potential to develop catalytic LIG-based surfaces for various applications, including contaminant removal and microbial inactivation.

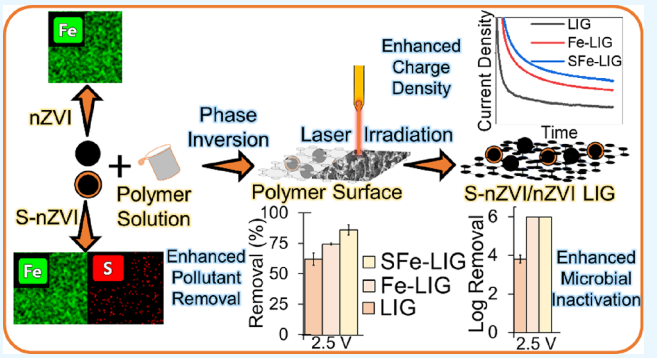

1. INTRODUCTION

The growing population, rapid urbanization, and industrialization have led to pollution of the water matrixes with various micropollutants and microorganisms. The increasing number of micropollutants in various water matrixes has grown worldwide concern due to the difficulty in their removal via conventional treatments; thus, it is required to use advanced treatment techniques.[1−3] One technique that has emerged as a promising treatment method is the electrochemical advanced oxidation process (EAOP).[1,2] The main mechanism of pollutant treatment in EAOP involves direct oxidation at the electrode's surface and indirect oxidation due to the generation of reactive oxygen species like hydrogen peroxide (H_2O_2).[1−4] The commonly used electrode materials for EAOP are dimensionally stable anodes (DSAs) and boron-doped diamonds (BDDs), which are cost extensive.[5−7] Graphene is a carbon-based nanomaterial with carbon atoms arranged in a hexagonal structure and extraordinary physicochemical properties.[8−11] The high electron and thermal mobility, exceptionally high surface area, and mechanical strength make it a good fit for electrochemical applications.[8−11] Many studies have introduced heteroatoms into graphene to enhance its catalytic properties.[12−16] The synthesis of pure graphene is tedious and expensive and also includes the usage of harmful chemicals.[13,17] Recently, facile method for graphene production have been developed by using laser irradiation of the carbonaceous substrate called laser-induced graphene (LIG).[18−20]

LIG is a facile, chemical-free, and single-step process of graphene formation on any carbon-containing surface using CO_2 infrared laser irradiation.[20,21] Over the past few years, its electrical, antibacterial, antibiofilm, and antibiofouling properties have been widely explored for various environmental applications, including electrochemical oxidation, adsorption, and sensors.[21−25] Recently, efforts have been made to alter/enhance the surface wettability and catalytic activity of LIG by tuning laser settings or heteroatom incorporation into the LIG matrix.[15,16,21,26,27] Heteroatoms include metals and nonmetals,

Received: January 30, 2024
Revised: April 21, 2024
Accepted: April 25, 2024
Published: May 13, 2024

and their incorporation effectively enhances the catalytic performances of LIG.[15,16,21,26,27] Many methods have been reported for heteroatom incorporation, including the use of direct laser irradiation in different atmospheric conditions on heteroatom-containing polymer surfaces.[26,28] Some have used polymers that contain useful heteroatoms in their molecular chain, like the presence of sulfur atoms in the polysulfone class of polymers, to fabricate sulfur-doped LIG surfaces.[21] Recently, studies have explored the incorporation of metal/metal oxides or electrocatalysts for enhancing electrochemical activity.[21,29−32] Recently, Kumar et al. fabricated Magnéli-Phase Ti_4O_7 LIG surfaces and showed improved anodic stability compared to the control LIG.[15] These heteroatom-incorporated LIG surfaces have also shown enhanced pollutant removal, bacterial inactivation, and virus inactivation by applying low voltages and antibiofilm and antibiofouling properties.[15,16,21,29−32]

Nanoparticle incorporation into the LIG surface has been demonstrated for enhanced antibacterial activity and pollutant removal.[15,33−36] One of the most studied nanomaterials for contaminant removal is the nanoscale zerovalent iron (nZVI) due to its high reactivity toward contaminant removal via adsorption and reductive and oxidative processes.[37] They have also been used in advanced oxidation processes due to their ability to produce hydroxyl radicals via reaction with hydrogen peroxide.[38,39] However, nZVI has poor selectivity for contaminants and a short reactive lifetime.[40] On the other hand, sulfidized nZVI (S-nZVI) has shown that sulfidation widens the range of reactive contaminants with increased selectivity and increases the reactive lifetime of nZVI by inhibiting undesirable reactions with water.[40−42] S-nZVI has also been shown to facilitate dechlorination and defluorination of the contaminants.[40−42] Iron-based nanoparticles have been used in Fenton technology as an AOP, which employs the generation of hydroxyl radicals (•OH) to degrade organic pollutants. However, the continuous addition of the Fenton reagent requires a mixture of Fe^{2+} and H_2O_2, resulting in iron sludge.[43−45] On the other hand, electro-Fenton has gained widespread attention due to its low toxicity, operation at neutral pH, and reduced sludge production.[43−45] It also eliminates the risk associated with handling and transporting H_2O_2 via the traditional Fenton process. In an electro-Fenton process, H_2O_2 is continuously generated at the cathode through two-electron reductions of O_2, which then reacts with Fe^{2+} to produce •OH. Moreover, Fe^{2+} regeneration can be done via direct cathodic or organic reduction.[43−45] However, no study has fabricated nZVI- and S-nZVI-incorporated LIG surfaces for the electro-Fenton process.

Hence, to combine the benefits of iron-based nanoparticles and LIG, we fabricated nZVI- and S-nZVI-incorporated LIG sheets and filters in this study. The sheets were first fabricated and characterized to confirm the successful incorporation of iron-based nanoparticles in the LIG matrix, to check their electrochemical performance as electrodes, and to optimize the nanoparticle concentration. The optimized nanoparticle loading was then used to make LIG-based filters for flow-through filtration, which are commonly used in water and wastewater treatment. The environmental applicability was demonstrated using methylene blue, bacteria, and virus removal. We demonstrate the enhanced MB removal by the nanoparticle-incorporated filters as compared to the control LIG. The iron-based nanoparticles incorporated in LIG filters were also demonstrated for the filtration of bacteria and viruses with enhanced microbial killing. These filters can be used to generate in situ radicals for advanced oxidation of pollutants and microorganisms. Such catalytic filter fabrication can help in developing a hybrid filtration system for various electrochemically advanced processes for environmental remediation.

2. MATERIALS AND METHODS

2.1. Materials and Instruments. Commercial poly(ether sulfone) (PES) powder (DKSH, India) was used for preparing sheets and filters with dichloromethane (DCM, 99.5%) solvent (Merck, India) and *N*-methyl-2-pyrrolidone (NMP) solvent (Honeywell, India). Sodium borohydride ($NaBH_4$), methylene blue stain (Merck, India), sodium dithionite ($Na_2S_2O_4$), and sodium sulfate (Na_2SO_4) were procured from Sigma-Aldrich, India. Tryptic soy broth (TSB), tryptic soy agar (TSA), and bacteriological agar were purchased from HiMedia. 0.22 μM bacteriological sterile filters were obtained from Axiva. $MgSO_4 \cdot 7H_2O$ and Tris buffer were procured from Loba Chemie Pvt., Ltd. *Escherichia coli* (*E. coli*) phage MS2 (ATCC 15597-B1) and its corresponding host *E. coli* C3000 (ATCC 15597) were procured from the American Type Culture Collection (ATCC).

Laser system VLS 2.30 (Universal Laser Systems), having a 10.6 μm CO_2 pulse laser of 30 W, 2.0 in. lens kit, was used for LIG fabrication. The sheets and filters were characterized with X-ray photoelectron spectroscopy-XPS (Kratos Analytical, AXIS Supra, UK), field emission gun-scanning electron microscopy (JEOL JSM-7600F, Japan), field emission gun-transmission electron microscopy having STEM and EDS mode (FEI Tecnai G2 F30, FEG-TEM 300 kV, USA), Fourier transform infrared-FTIR Spectroscopy (PerkinElmer, FTIR Spectrum 3, USA), and Raman spectroscopy (WITec, Alpha 300 Raman spectrophotometer, Germany) with a laser light source at 532 nm wavelength. A high-resolution X-ray diffraction (XRD) system (SmartLab, Rigaku diffractometer, Japan) was used for nanoparticle characterization. Contact angle measurements were made using an optical tensiometer (DSA25S, Kruss, Germany).

2.2. nZVI and Sulfidized-nZVI Preparation. The nZVI and sulfidized nano zerovalent iron (S-nZVI) nanoparticles were synthesized by the borohydride reduction method, as reported in previous studies.[40,46,47] Briefly, a 100 mL mixture of 34 $g \cdot L^{-1}$ $NaBH_4$ and 2.2 $g \cdot L^{-1}$ $Na_2S_2O_4$ were dropwise added to 100 mL of 10 $g \cdot L^{-1}$ Fe^{3+} solution under continuous mixing with nitrogen purging. The mixed solution volume and concentrations theoretically provide S-nZVI with a 0.14 S/Fe molar ratio. For the nZVI synthesis, the same method was used without adding $Na_2S_2O_4$. The resulting nanoparticle suspensions were then centrifuged at 5000 rpm for 10 min, and the supernatant was discarded. The remaining nanoparticles were washed with DI once and ethanol twice with the same centrifugation process. The centrifuge tubes containing the nanoparticles were then blown with gentle nitrogen gas flow for 10−15 min and then dried in a vacuum oven for 3 h. The nanoparticles were then stored in sealed vials until further use.

2.3. Fabrication of LIG, Fe-LIG, and SFe-LIG Sheets. The polymer sheets and filters were fabricated based on our previous study.[15,16] Briefly, 2.65 g of PES polymer was mixed with 22 mL of DCM under continuous stirring at 300 rpm. The solution was mixed for 15−20 min to get a homogeneous solution. The iron nanoparticle-incorporated solution was prepared by adding nZVI and S-nZVI nanoparticles in 2.5, 5, and 10 wt % of polymer. The suspension was then probed and

https://doi.org/10.1021/acsomega.4c00959
ACS Omega 2024, 9, 22819−22830

sonicated for 5 min to get a uniform suspension. The mixed suspension was then poured into a Petri dish with a 14.5 cm inner diameter. An inverted funnel was placed over the Petri dish for controlled evaporation of DCM. After 6 h, the solidified PES and nanoparticle-incorporated sheets were removed gently from the glass plate. For the LIG sheet fabrication, double-sided tape was used to fix the sheets on the laser platform. The sheets were laser irradiated to get an electrode area of 3 × 1 cm^2, under ambient conditions at an optimized setting of image density 6, 150 pulses per inch, 15% power, and 25% rastering speed with z = 0.2 mm. The LIG fabricated on PES, nZVI, and S-nZVI incorporated sheets were named LIG, Fe-LIG, and SFe-LIG sheets, respectively.

2.4. Fabrication of LIG, Fe-LIG, and SFe-LIG Filters. The fabrication of LIG was similar to that reported in our previous studies.[15,27,48] First, PES membranes were fabricated via the phase inversion method using 15% (w/v) PES in NMP solution. For fabricating nZVI- and S-nZVI-incorporated membranes, 10% (wt of PES) nanoparticles were mixed into the 10 mL polymer solution. The solution was then probe-sonicated and mixed for 5 min. The mixed solution was then poured onto an NMP-wiped polyester support fixed to a glass plate. The casting blade positioned for 290 μm total thickness was immediately moved over the poured solution. After 30 s, the whole glass plate was immersed in a water bath for membrane formation, which was then kept in water until LIG formation. For the formation of the LIG on the membranes, the membranes were moved out of the water bath, dried, and fixed on the laser platform. The active side of the fixed membranes was then irradiated with a 10.2 μm CO_2 laser at 10% power, 25% speed, 0.2 mm z distance, 1000 pulse per inch (PPI), and image density (ID) of 6. The filters obtained from the PES membrane and nZVI- and S-nZVI-incorporated membranes were named LIG, Fe-LIG, and SFe-LIG filters, respectively.

2.5. Electrochemical Characterization. The electrochemical characterization of the LIG filters/electrodes was done using cyclic voltammetry (CV) and chronoamperometry (CA) in a three-electrode system using a potentiostat (AUT.MAC204.S, Metrohm Autolab, India) with 0.05 M Na_2SO_4 as the background electrolyte. The LIG, Fe-LIG, and SFe-LIG filters of 1 cm^2 were used as working electrodes, the platinum coil was used as a counter electrode, and the reference electrode was a calomel electrode (SCE, 0.241 V vs RHE). CV was recorded for the filters at 0.1 $V{\cdot}s^{-1}$ scan rate, and the CA was recorded at 1.5 V vs SCE. The anodic stability of the filters was checked via performing CV from 0 to 2.5 V for 60 cycles.[4,49] Under anodic potential, electroconductive membranes (ECMs) can undergo electro-oxidation themselves; hence, checking the anodic stability of ECMs is important. On the other hand, the ECMs maintain their stability under cathodic potential and are not investigated.[4,49,50] Moreover, electrochemical impedance spectroscopy (EIS) was done in the 100 kHz to 0.1 Hz frequency range with 7 mV rms amplitude.

2.6. Methylene Blue Removal by LIG-Based Filters. The performance of the fabricated LIG for removing micropollutants was tested by using methylene blue (MB) dye. The tests were carried out using two filters in a stack configuration in dead-end mode, each acting as anode and cathode, respectively (Figure S1). Electrical connections were made using carbon thread and conductive paste. The connections were then secured with an epoxy coating. The experiments were done in dead-end mode with a 500 mL feed of 10 ppm of MB at a flow rate of ∼1000 LMH with the application of 2.5 V. The permeate was recirculated back to the feed to maintain a constant volume. Samples from the feed, as well as permeate, were taken at different times for MB quantification using a UV−vis spectrophotometer at a 665 nm wavelength. The reusability of the filters was tested for three runs of 3 h each with a fresh feed of 10 ppm MB. The electrogeneration of H_2O_2 was assessed at 2.5 V both in the absence and in presence of the hydroxyl radical scavenger *tert*-butanol. Samples were collected from the permeate, and the concentration of H_2O_2 was determined using the DMP method.[51]

2.7. Bacterial and Virus Inactivation by LIG, Fe-LIG, and SFe-LIG Filters. *Electrochemical Inactivation of Bacteria.* The bacterial filtration tests were performed against mixed bacterial cultures as performed in the previous studies.[15,27] In brief, the mixed culture of bacteria was extracted from the nearby Powai Lake in Mumbai, India. The culture was revived in nutrient broth overnight, centrifuged, and washed three times with a 0.9% NaCl solution. The obtained suspension was diluted to form ∼10^6 $CFU{\cdot}mL^{-1}$ for filtration experiments. The filtration experiments were performed in a vacuum filtration assembly with stacked LIG, Fe-LIG, and SFe-LIG filters,[15] with the filtration flow rate maintained at ∼500 LMH.

MS2 Phage Propagation. The stock solution of the MS2 phage was prepared as per the protocol mentioned in the previous study.[1] Briefly, the host *E. coli* C3000 was allowed to grow until the exponential phase (OD_{600} = 0.6−0.8) in TSB at 37 °C and then 300 μL of the host was added to 100 μL of the phage. Furthermore, soft agar (0.5% w/v of TSA) was added to this phage−host mixture and overlaid onto the bottom agar (1.5% w/v of TSA) and incubated at 37 °C. The propagated phages were purified wherein suspension medium buffer was added onto the completely lysed plates and kept under shaking conditions for 2−3 h at 4 °C. The suspension was collected and centrifuged (16,000 rpm, 30 min), and then the supernatant was passed through 0.22 μM bacteriological filters to obtain purified MS2 stock (10^{10} $PFU{\cdot}mL^{-1}$). The purified stocks were adjusted to a concentration of 10^6 $PFU{\cdot}mL^{-1}$ for further experiments.

Electrochemical Inactivation of MS2 Phage. The LIG and doped LIG filters were checked for their antiviral activity in the flow-through condition using a dead-end vacuum filtration setup as described in the previous studies.[1,2] Briefly, the filters were stacked with an anode on top and a cathode at the bottom configuration and were connected to the DC power supply. At a constant flow rate of ∼500 LMH, 30 mL of MS2 solution (10^6 $PFU{\cdot}mL^{-1}$) in 0.9% NaCl was passed through these filters at varying voltage ranges (0−5 V). 300 μL of the sample was collected from the filtrate and quantified using the double-layer agar method.[3]

The log removal (L) for the bacteriophages was calculated using eq 1:[4]

$$L = -\log(C/C_0) \quad (1)$$

where C and C_0 are concentrations of phages after and before treatment, respectively.

3. RESULTS AND DISCUSSION

3.1. LIG, Fe-LIG, and SFe-LIG Sheet Characterization. The iron nanoparticles, including nZVI and S-nZVI, were

https://doi.org/10.1021/acsomega.4c00959
ACS Omega 2024, 9, 22819−22830

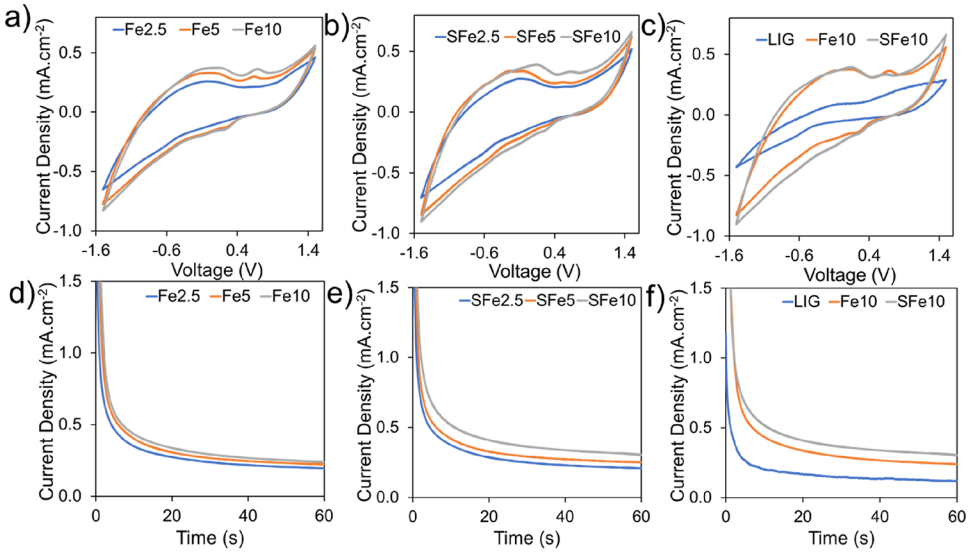

Figure 1. Cyclic voltammogram of LIG sheets with different concentrations of (a) SFe and (b) Fe. (c) Cyclic voltammogram of control LIG and 10% nanoparticle-incorporated LIG sheets. Chronoamperograms at 2.5 V for different concentrations of (d) Fe and (e) SFe. (f) Chronoamperograms at 2.5 V of control LIG and 10% nanoparticle-incorporated LIG sheets.

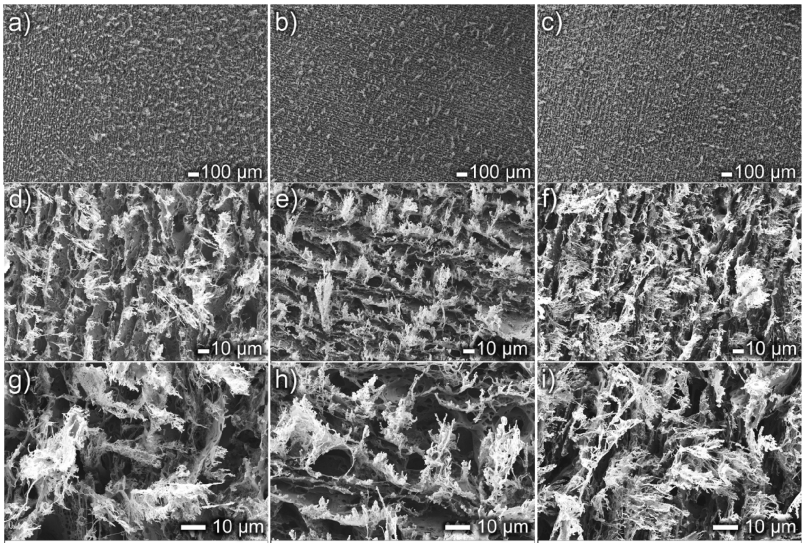

Figure 2. SEM images at 100×, 1000×, and 2500× magnifications of LIG (a, d, g), Fe-LIG (b, e, h), and SFe-LIG sheets (c, f, i).

synthesized using the previously reported borohydride reduction method.[40,46,47] The synthesized nanoparticles were characterized by XRD and TEM-EDS mapping. The XRD diffractograms of nZVI and S-nZVI are shown in Figure S2a. The nZVI showed the characteristic diffraction peak of Fe^0 at $2\theta = 44.7°$ corresponding to the body-centered cubic structure. Peaks in the nZVI diffractogram at 44.7, 65.0, and 82.3° are attributed to Fe (PDF 00-006-0696). For S-nZVI, the diffractogram showed various peaks at 29.9, 35.9, 44.7, 57.4, 63.0, 65.4, and 82.3° and matched with FeS (PDF 01-089-6928), indicating the sulfidization of the nZVI nanoparticles. TEM-EDS mapping shows the presence of iron in nZVI and S-nZVI (Figure S2b−e,g,h). The presence of sulfur can also be seen in S-nZVI (Figure S2f,i), indicating that S scattered throughout the Fe region (Figure S2e,f,h,i). Apart from iron and sulfur, oxygen was also present in the synthesized nanoparticles of nZVI and S-nZVI (Figure S3 and Table S1), suggesting the surface oxidation of these iron nanoparticles.[40,46]

The nZVI and S-nZVI nanoparticles were used to fabricate LIG sheets at various nanoparticle concentrations of 2.5, 5, and 10%. The electrochemical characterization of these LIG, Fe-LIG, and SFe-LIG sheets was performed using CV and CA. CV and CA were recorded for different concentrations of nanoparticles, i.e., 2.5, 5, and 10%. The CV curves of the Fe-LIG and SFe-LIG sheets showed redox peaks, which were distinctly visible at higher nanoparticle concentrations of 10% (Figure 1a,b).[44,52] This ensures the presence of iron within the system, which can help in pollutant degradation during electrochemical treatments. Also, Fe-LIG and SFe-LIG sheets with 10% nanoparticle incorporation showed higher current responses than 2.5 and 5% (Figure 1a,b), indicating their higher conductivity. Charge density (C) indicates the sheets' electrochemically active surface area and electrochemical

https://doi.org/10.1021/acsomega.4c00959
ACS Omega 2024, 9, 22819−22830

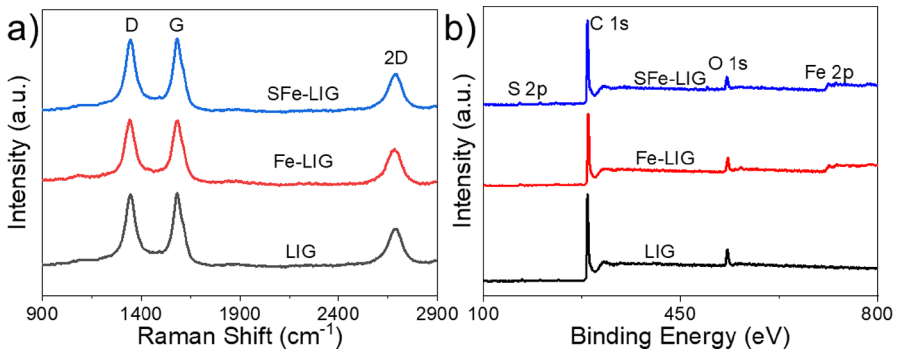

Figure 3. (a) Raman spectra of LIG, Fe-LIG, and SFe-LIG sheets. (b) XPS spectra of LIG, Fe-LIG, and SFe-LIG sheets.

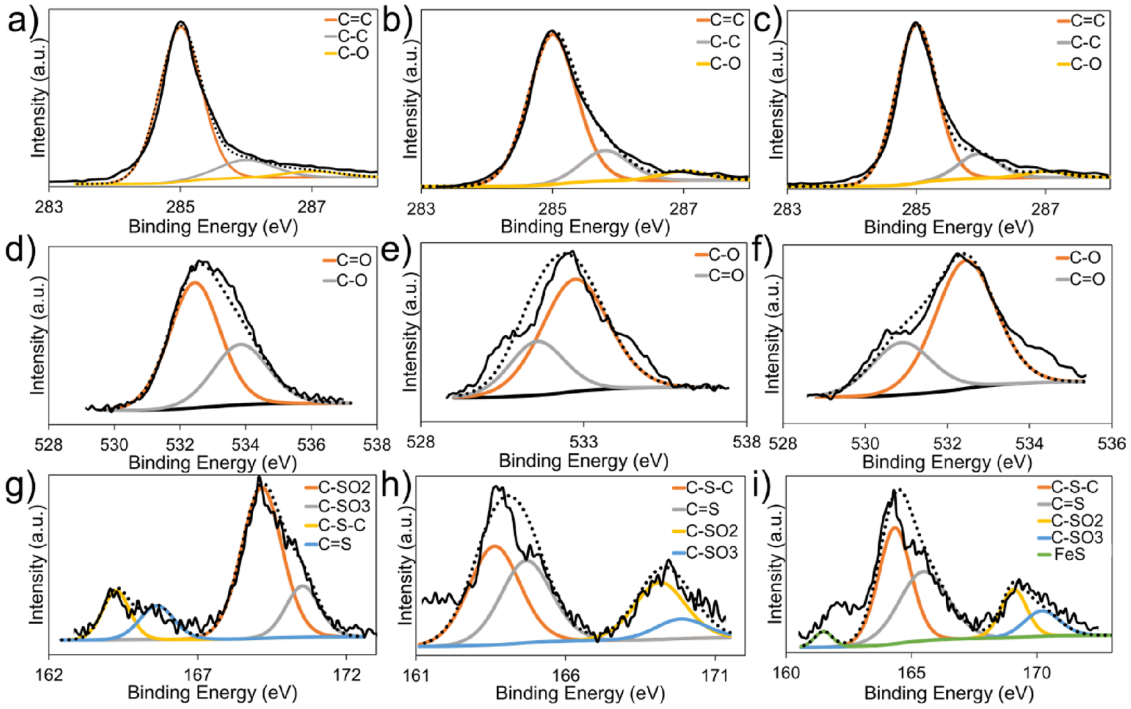

Figure 4. C 1s deconvolution of sheets (a) LIG, (b) Fe-LIG, and (c) SFe-LIG. O 1s deconvolution of (d) LIG, (e) Fe-LIG, and (f) SFe-LIG sheets. S 2p deconvolution of (g) LIG, (h) Fe-LIG, and (i) SFe-LIG sheets. The black solid line and black dotted line represent the XPS spectrum and fitted curve, respectively.

activity. C is proportional to the CV curve area and was calculated using eq 2:[15,53,54]

$$C = \frac{\int IdV}{v} (\mu C \cdot cm^2) \tag{2}$$

where $\int IdV$ is the CV curve area and v is the scan rate. The charge densities for 2.5, 5, and 10% nZVI-incorporated Fe-LIG sheets were calculated to be 0.81, 1.06, and 1.13 × 10^4 μC·cm^2, respectively. Similarly, SFe-LIG sheets gave C values of 0.94, 1.2, and 1.32 × 10^4 μC·cm^2 for 2.5, 5, and 10% S-nZVI incorporation, respectively. The CV response of LIG with 10% nanoparticle incorporation is compared in Figure 1, which clearly shows a better response of the nanoparticle-incorporated Fe-LIG and SFe-LIG sheet as compared to the LIG sheet. The charge density of LIG was 0.4 × 10^4 μC.cm^2, much lower than those of nanoparticle-doped LIG sheets (Figure 1c). 10% nanoparticle-incorporated Fe-LIG and SFe-LIG sheets had 2.85 and 3.33 times greater charge density than LIG sheets, indicating their higher potential for electrochemical activity.[15,16] Figure 1d,e shows the chronoamperogram of the sheets recorded at 2.5 V vs SCE in 0.05 M Na_2SO_4 solution. The current density reduced during ∼15 s in all the sheets due to the concentration relaxation effect and reached a steady state.[15,55] The 10% incorporated Fe-LIG and SFe-LIG sheets showed higher current density as compared to 2.5 and 5% nanoparticle incorporation. Compared to LIG, Fe-LIG and SFe-LIG sheets with 10% nanoparticle incorporation showed a higher current density (Figure 1f). Considering the electrochemical responses, the SFe-LIG sheet responded better than the Fe-LIG and LIG sheets. For all further characterization, results, and discussion, 10% nanoparticle-incorporated Fe-LIG and SFe-LIG were used, as they performed better than 2.5 and 5% nanoparticle-incorporated sheets (Figure 1).

The SEM images of the sheets were taken at different magnifications of 100×, 1000×, and 2500× (Figure 2). Due to laser irradiation, the sheet surface turned into a highly porous forest-like structure (Figure 2a−c) due to the rapid release of gaseous products.[23,56] The fibrous structures for LIG, Fe-LIG, and SFe-LIG are also clearly visible in Figure 2d−i. Such

https://doi.org/10.1021/acsomega.4c00959
ACS Omega 2024, 9, 22819−22830

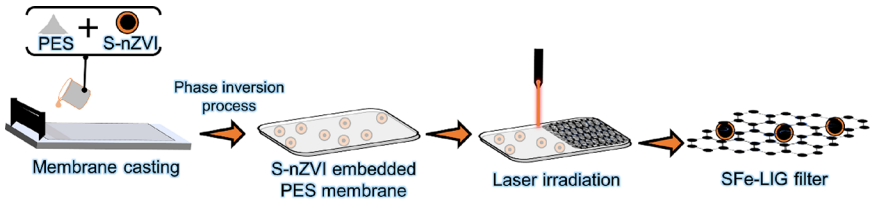

Figure 5. Schematic showing the fabrication process of the SFe-LIG filter.

forest-like porous and fibrous structures have also been reported in previous LIG fabrication studies.[14,15,21,31] For elemental analysis, SEM-EDS of the LIG, Fe-LIG, and SFe-LIG sheets has also been done (Figures S4–S6). As shown in Figure S4, LIG sheets are composed of mainly carbon, oxygen, and sulfur. SEM-EDS of Fe-LIG and SFe-LIG also showed similar elemental composition with additional iron peaks due to nZVI and S-nZVI incorporation, respectively (Figures S5 and S6). The sheets also showed the characteristic peak bands of graphene in the Raman spectrum, including the defect or disorder-induced D band, first-order allowed G band, and the 2D band coming from the second-order zone-boundary phonons[20,23,57] (Figure 3a). These D, G, and 2D bands are observed at Raman shifts of ∼1350, ∼1580, and ∼2700 cm^{-1}, respectively. The D band is commonly observed near the sample edges or due to disordered samples. The first-order Raman scattering process results in the G band and is related to the doubly degenerate mode at the Brillouin zone center. The 2D band is observed approximately at twice the D band and is allowed in the second-order Raman spectra of graphene. The 2D peaks of all three LIG, Fe-LIG, and SFe-LIG sheets can be fitted with only one Lorentzian peak having a full width at half-maximum of 94.4 ± 2.37, 89.6 ± 1.4, and 85.0 ± 1.1 cm^{-1}, respectively, indicating turbostratic graphene (Figure S7).[18−20,23,57] X-ray photoelectron spectroscopy (XPS) gives information on the elemental composition of the material's surface. The spectrum showed the C 1s, O 1s, and S 2p peaks at ∼285, ∼534, and ∼167 eV, respectively (Figure 3b), indicating that the sheets were mostly composed of carbon, oxygen, and sulfur.[21,23] However, just like the EDS spectra (Figures S5 and S6), the XPS spectra of Fe-LIG and SFe-LIG also showed peaks of Fe at ∼705−735 eV, confirming the successful incorporation of nZVI and S-nZVI into the sheet matrix. The concentrations of nZVI and S-nZVI as Fe in Fe-LIG and SFe-LIG sheets were ∼9.4 ± 1.3% mass concentration (Table S2).

The XPS deconvolution of the C 1s, O 1s, and S 2p narrow spectra of LIG, Fe-LIG, and SFe-LIG sheets is shown in Figure 4. The C 1s contained mostly the C═C, C−C, and C−O bonds (Figure 4a−c), with a major contribution coming from C═C (∼79−84%), followed by C−C (∼13−16%) and C−O (∼3−5%).[15,16,21,58] The O 1s spectra contained the two major peaks of C═O and C−O (Figure 4d,e), with C═O being the major contributor of ∼66−72% and the rest coming from C−O (∼29−34%).[15,16,21,58,59] The deconvolution of S 2p majorly showed bonding of C-SOx (∼13−59%), C═S (11−35%), and C−S−C (∼13−39%), respectively, indicating the incorporation of sulfur in graphene, as has been shown previously for poly(ether sulfone) based LIG fabrication studies.[15,16,21,58,59] Additionally, for the SFe-LIG sheet, S 2p deconvolution showed a peak at ∼161.5 eV, which corresponds to FeS, thus further confirming the presence of S-nZVI in the SFe-LIG sheets.[60,61] The Fe 2p of Fe-LIG and SFe-LIG sheets was also deconvoluted, as shown in Figure S8. The peaks ∼707 eV correspond to Fe(0) related to nZVI species.[62,63] The peak at ∼711 (Fe $2p_{3/2}$) can be attributed to Fe(II), while the peaks at ∼713 (Fe $2p_{3/2}$) and ∼725 eV (Fe $2p_{1/2}$) assigned to Fe(III) (Figure 5a,b).[62,64,65] The peaks at ∼719−721 eV are satellite peaks of Fe[62,64,66] (Figure 5a,b), while the peak at ∼716 eV in the case of SFe-LIG (Figure 5b) corresponds to FeS coming from the S-nZVI incorporation.[64,67] Taking the sheets' characterization, it is clear that the incorporation of iron nanoparticles into LIG sheets was successful.

3.2. LIG, Fe-LIG, and SFe-LIG Filter Fabrication and Characterization. Since 10% nanoparticle incorporation gave better electrochemical activity in sheets as compared to 2.5 and 5%, hence, for filter fabrication, a 10% nanoparticle concentration was used. The nanoparticles were first used to make PES membranes via a phase inversion process, followed by laser irradiation to convert them into nanoparticle-incorporated LIG filters (Figure 5). The control LIG filter fabrication was done without nanoparticle addition. The SEM images of LIG (Figure 6a,d,g), Fe-LIG (Figure 6b,e,h), and

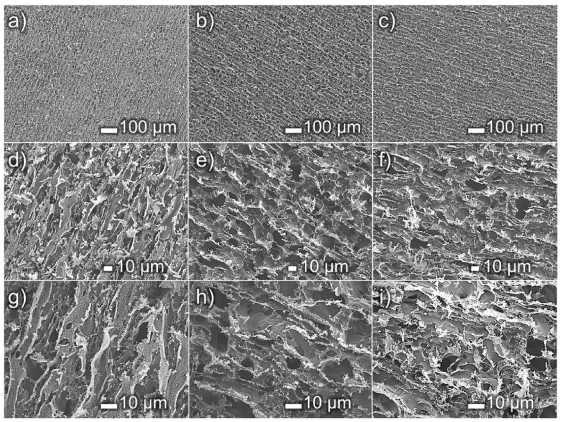

Figure 6. SEM images at 100×, 500×, and 1000× magnification of LIG (a, d, g); Fe-LIG (b, e, h); and SFe-LIG filters (c, f, i).

SFe-LIG filters (Figure 6c,f,i) at various magnifications are shown in Figure 6. Similar to the sheets, the filter's surface turned into a forest-like, highly porous, and fibrous structure, as discussed in previous LIG fabrication studies.[14,15,21,31]

The EDS mapping for filters showed the presence of carbon as well as iron (Figure 7a−f) in both Fe-LIG and SFe-LIG. The carbon is mainly from the graphene, whereas the iron is from the nanoparticles incorporated into the filters. A scattered pattern of sulfur was also seen in most places of iron, indicating the presence of S-nZVI in the SFe-LIG filter (Figure 7g), although sulfur from the LIG matrix can also contribute to sulfur seen in Figure 7g. Figure S2d,i confirms that the FeS nanoparticles have Fe as well as S. Incorporating FeS in LIG showed the presence of Fe in Figure 7f, which will be

https://doi.org/10.1021/acsomega.4c00959
ACS Omega 2024, 9, 22819−22830

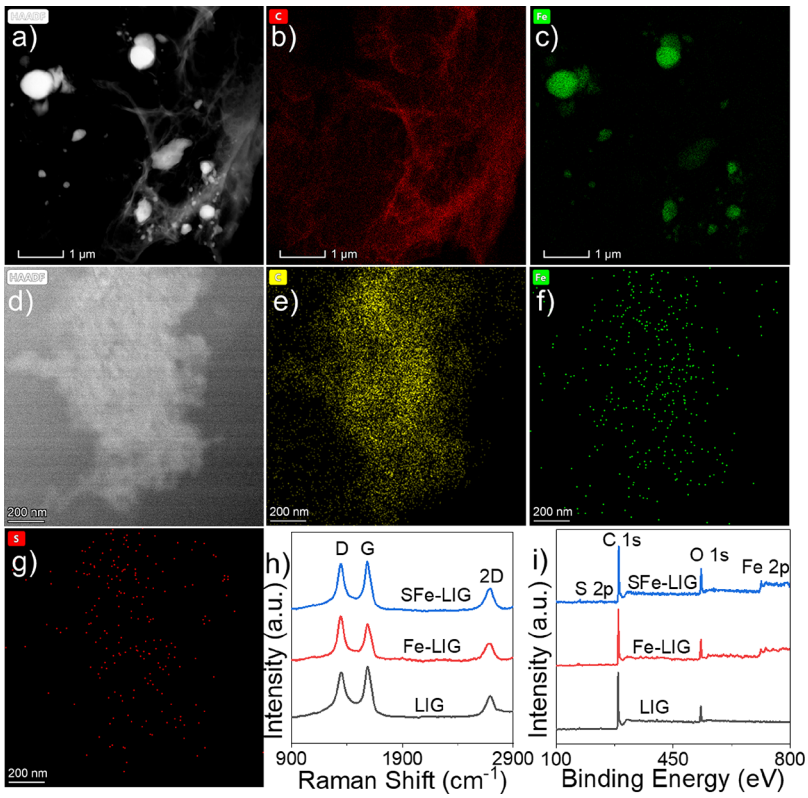

Figure 7. Filter characterization: TEM-EDS mapping of (a–c) Fe-LIG and (d–g) SFe-LIG; (h) Raman spectra of LIG-based filters; (i) XPS spectra of LIG-based filters.

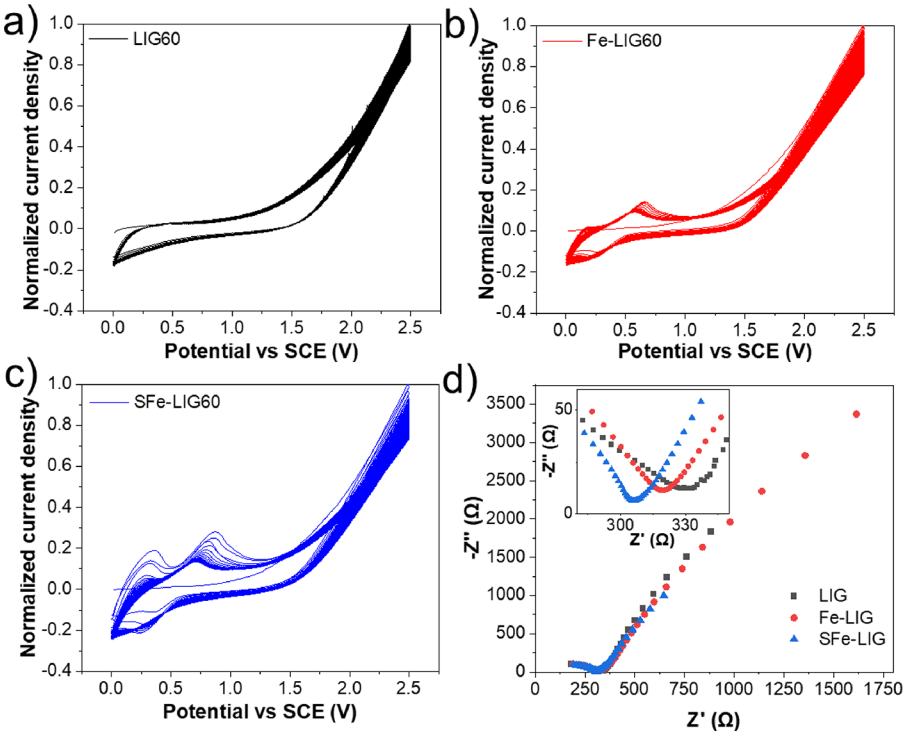

Figure 8. Cyclic voltammograms for 60 cycles anodic stability of (a) LIG, (b) Fe-LIG, and (c) SFe-LIG filters. (d) Nyquist plot of filters.

accompanied by the S part of the FeS (Figure S2d–i). Thus, both nanoparticles were incorporated into the filter matrix. Additionally, EDS elemental mapping of the SFe filter's surface was done to see the distribution of iron on the filter's surface, which showed that the nanoparticles were evenly distributed on the LIG matrix (Figure S9). The sizes of iron-based nanoparticles were ~70–80 nm similar to our previous study.[47] The hydrophilicity of the filters was measured by using the contact angle measurement and was found to be hydrophilic with a contact angle of ~75° (Figure S10). The

https://doi.org/10.1021/acsomega.4c00959
ACS Omega 2024, 9, 22819–22830

FTIR spectrum of PES and nanoparticle-incorporated membranes before laser irradiation is shown in Figure S11, all of which matched with the poly(ether sulfone) polymer. Upon laser irradiation, the FTIR spectrum for LIG filters (Figure S11) showed a peak between ∼1600 and 2000 cm^{-1}, which can be attributed to C═O stretching, and the spectra are similar to the LIG filters reported earlier.[68] Raman spectra of LIG, Fe-LIG, and SFe-LIG filters (Figure 7h) showed the characteristic peak bands of graphene D, G, and 2D bands at Raman shifts of ∼1350, ∼1580, and ∼2700 cm^{-1}, respectively,[20,23,57] thus indicating the successful fabrication of graphene on these surfaces.[15,21] The 2D peaks were also fitted with one Lorentzian peak with full widths at half-maximum of 91.2 ± 1.7, 92.8 ± 2.8, and 90.0 ± 1.4 cm^{-1} for LIG, Fe-LIG, and SFe-LIG filters, respectively, indicating turbostratic graphene (Figure S12).[18−20,23,57] The XPS spectra of LIG-based filters (Figure 7i) showed peaks of C, O, and S at ∼285, ∼ 534, and ∼167 eV, respectively, with additional Fe peaks at ∼705−735 eV for Fe-LIG and SFe-LIG filters. The deconvolution of the narrow peaks of these filters is also provided in Figures S13 and S14. The C 1s bonds contained mostly the C═C, C−C, and C−O bonds, with a major contribution coming from C═C (∼78−85%). The O 1s spectra contained the two major peaks of C═O (∼55−82%) and C−O (∼18−45%). The deconvolution of S 2p majorly showed bonding of C-SOx (∼51−66%), C═S (11−24%), and C−S−C (∼20−25%), respectively, which is mostly from the sulfur embedded in the PES polymer chain.[21] Additionally, S 2p deconvolution for the SFe-LIG filter showed a peak at ∼161.5 eV, which corresponds to FeS,[60,61] confirming the successful incorporation of S-nZVI. The Fe 2p deconvolution for Fe-LIG and SFe-LIG filters (Figure S14) showed peaks corresponding to Fe(0), Fe(II), satellite peak, and Fe(III). The peak at ∼716 eV in the case of the SFe-LIG filter can be attributed to FeS.[64,67] Based on the characterization results, we can say that the filters were successfully incorporated with the iron-based nanoparticles nZVI and S-nZVI.

The electrochemical characterization of the filters was also performed using CV, CA, anodic stability tests, and EIS. The Fe-LIG and SFe-LIG filters showed ∼1.7 and ∼2.2 times higher electrochemical activity with charge densities of 1.77 and 2.26 × 10^4 $\mu C \cdot cm^2$, respectively, as compared to 1.03 × 10^4 $\mu C \cdot cm^2$ of LIG (Figure S15a). The anodic stability of the filters was also measured over 60 CV cycles from 0 to 2.5 V (Figure 8a−c). The normalized current density decreased by ∼20−25% for the LIG, Fe-LIG, and SFe-LIG filters. This is due to the drop in the electrical conductivity of the filters under continuous anodic potential, which likely resulted in the LIG oxidation and breakdown.[30,49,69] Figure S15b shows the chronoamperogram of the filters recorded at 1.5 V vs SCE in 0.05 M Na_2SO_4 solution. SFe-LIG showed a higher current density as compared to other filters. EIS was performed to probe the charge transfer resistance of the filters (Figure 8d). It can be seen from Figure 8d that SFe-LIG has the smallest semicircle diameter, indicating lower charge transfer resistance. This aligns with the literature that sulfidation lowers the charge transfer resistance and facilitates electron transfer.[40,46,70] Thus, based on the electrochemical characterization, we can say the incorporation of nZVI and S-nZVI has enhanced the electrochemical activity of the LIG-based filters. Furthermore, SFe-LIG shows the best electrochemical CV and CA response with the lowest charge transfer resistance compared to LIG and Fe-LIG filters.

3.3. Environmental Application of LIG, Fe-LIG, and SFe-LIG Filters. The application of 10% iron nanoparticles incorporated in LIG-based filters was demonstrated by using an MB removal study. The removal was investigated in continuous permeate recirculated dead-end mode. Samples were taken from both the permeate and feed at different time intervals to quantify the MB concentration. As shown in Figure 9a, removal in permeate was ∼40, ∼50, and ∼70% within 15

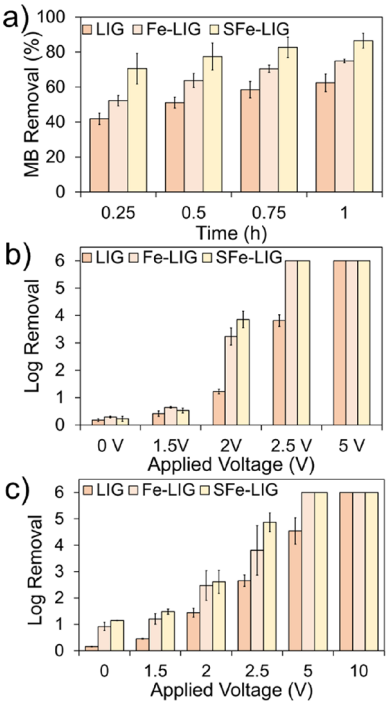

Figure 9. LIG, Fe-LIG, and SFe-LIG filter's removal performance for (a) methylene blue, (b) bacteria, and (c) virus. Methylene blue removal was performed with a 2.5 V application.

min for LIG, Fe-LIG, and SFe-LIG filters, respectively. After 1 h, the MB removal was ∼60, ∼70, and ∼90% for LIG, Fe-LIG, and SFe-LIG filters, respectively. The enhanced removal of MB by SFe-LIG filter as compared to LIG and Fe-LIG filters is due to the enhanced electrochemical activity and charge density (Figures 1 and 8). The increase in removal performance by the iron nanoparticle-incorporated filters is due to improved electrochemical interaction of Fe-LIG and SFe-LIG filters with MB molecules, *in situ* generation of hydroxyl radicals due to electro-Fenton process, and direct oxidation.[4,45,71,72] Moreover, Fe^{2+} regeneration can take place via direct cathodic reduction.[43−45]

LIG, Fe-LIG, and SFe-LIG filters were also investigated and compared for their bacterial and virus inactivation under the application of various voltages (0−10 V). At 0 and 1.5 V, less than one log removal of bacteria was observed (Figure 9b) mostly due to adsorption and electroadsorption.[14−16,29] Similar observations were made for the virus removal for 0 and 1.5 V (Figure 9c).[14−16,29] With the increase in applied voltage, bacterial removal increased for the filters with ∼1-, 3-, and 4-log removal at 2 V by the LIG, Fe-LIG, and SFe-LIG filters. At 2.5 V, LIG only showed ∼4-log removal while the Fe-LIG and SFe-LIG filters showed 6-log removal. LIG filters required a higher voltage of 5 V to show 6-log removal, while 2.5 V was enough for the iron-incorporated filters to show the same

https://doi.org/10.1021/acsomega.4c00959
ACS Omega 2024, 9, 22819−22830

removal, showing the potential of iron nanoparticle incorporation. Similarly, ∼1.5−3 log removal of the virus was observed for LIG filters while enhanced removal of ∼2.5−5-log removal was obtained for Fe-LIG and SFe-LIG filters at 2 and 2.5 V, respectively. At the application of 5 V, complete 6-log removal of virus was observed with Fe-LIG and SFe-LIG filters while only ∼4.5-log removal was observed with LIG filters. This clearly shows that Fe-LIG and SFe-LIG filters outperform the LIG filters, which were able to show complete virus removal only at a higher voltage of 10 V.

The bacterial and virus removal by the LIG filters can be attributed to the physical destruction by the LIG surface, electrochemical interaction between microorganisms and the electrode surface, direct oxidation, and indirect oxidation via reactive species generation (H_2O_2). The enhanced removal by the Fe-LIG and SFe-LIG filters, as compared to that by LIG filters, can be attributed to the enhanced electrochemical activity and response, as discussed earlier (Figures 1 and 8 and Figure S15). Additionally, the Fe-LIG and SFe-LIG filters cause *in situ* generation of •OH due to the electro-Fenton process, which has a more potent oxidizing potential than H_2O_2.[43,45] The continuous electro-generation of H_2O_2 and thus •OH in the case of Fe-LIG and SFe-LIG eliminates the requirement and risk associated with H_2O_2 handling and transporting in the Fenton process. Moreover, Fe^{2+} regeneration can be done via direct cathodic or organic reduction.[43−45] Thus, both nZVI and S-nZVI present in the LIG matrix of Fe-LIG and SFe-LIG filters are capable of producing •OH via the electro-Fenton process and hence were able to provide 6-log inactivation of bacteria and viruses at lower voltages as compared to LIG filters. However, as the voltage applied increased, complete inhibition was observed for all the filters due to the predominant electrical effect at high voltage and electrochemical oxidation.[14−16,58,73] Nevertheless, the enhanced electrochemical effect of Fe-LIG and SFe-LIG filters can enhance the pollutant and microbial removal performance as compared to that of LIG filters.

The incorporation of iron-based nanoparticles into the LIG matrix enhances its electrical conductivity, as evidenced by the surface resistance comparison (Figure S16a). The surface resistance of LIG filters was ∼75 $\Omega\cdot sq.^{-1}$, whereas Fe-LIG/SFe-LIG filters exhibit a reduced surface resistance of ∼35−40 $\Omega\cdot sq.^{-1}$, leading to improved electrical conductivity (Figure 8 and Figure S15). Moreover, CA responses and CV curve areas reveal ∼2 times greater charge densities for Fe-LIG and SFe-LIG filters compared with LIG alone, indicating enhanced electrochemical activity and conductivity. Furthermore, the redox peaks observed in the CV curves of Fe-LIG and SFe-LIG surfaces (Figure 8 and Figure S15) suggest the occurrence of redox reactions, facilitating hydroxyl radical generation. This inference is corroborated by H_2O_2 measurements (Figure S16b), where LIG displays a concentration of ∼3.5 $mg\cdot L^{-1}$, whereas Fe-LIG and SFe-LIG filters exhibit reduced concentrations of ∼2.5 $mg\cdot L^{-1}$. The H_2O_2 generation with LIG composites can be attributed to its electroconductive nature and electroreduction capability, which can be steered with topological defects.[74,75] Notably, in the presence of the hydroxyl radical scavenger *tert*-butanol, all filters demonstrate a similar concentration of ∼3.5 $mg\cdot L^{-1}$ of H_2O_2. This underscores the role of the hydroxyl radical generation in Fe-LIG and SFe-LIG filters. Moreover, when compared to the control LIG filters, Fe-LIG/SFe-LIG filters exhibit superior performance in MB removal and microbial inactivation, with the control LIG showing 10−30% less MB removal and 2−3 log lower microbial inactivation. This substantiates the contribution of iron-based nanoparticles to the enhanced performance observed in the filtration process.

Since Fe-LIG and SFe-LIG filters outperformed LIG filters, we tested and compared the reusability of Fe-LIG and SFe-LIG filters for three cycles of longer filtration time (3 h) (Figure S17). The MB removal performance of Fe-LIG filters decreased from ∼93 to ∼77 and 70% in cycles 2 and 3, respectively (Figure S17a). Similarly, SFe-LIG also showed a decrease in MB removal performance from ∼93 to ∼90 and 81% in cycles 2 and 3, respectively (Figure S17b). The decrease in MB removal performance was less in the case of SFe-LIG filters as compared to Fe-LIG filters. Fe-LIG filters showed ∼17 and ∼25% decreases in the MB removal at the end of the second and third cycles, respectively, while SFe-LIG filters showed only ∼3 and ∼13% decrease in the MB removal at the end of the second and third cycles, respectively. This is due to the enhanced reactive lifetime of the S-nZVI of SFe-LIG filters as compared to the nZVI of Fe-LIG filters. Previous studies have shown that sulfidation of nZVI decreases its reactivity with water and increases its reactive lifetime.[46,65] Thus, the sulfidation of nZVI and the S-nZVI incorporation into the LIG filters can improve the electrochemical activity and enhance the contaminant removal with good reusability compared to Fe-LIG filters. It is important to mention that these catalytic ECMs can be recycled or regenerated using various methods explored in literature including electrodeposition, electroreduction, and regeneration of catalytic surfaces.[48,76,77]

4. CONCLUSIONS

We successfully fabricated nZVI- and S-nZVI-incorporated LIG surfaces in the present work. The electrochemical characterization showed that increases in nZVI and S-nZVI concentrations increased charge density and electrochemical activity. Fe-LIG and SFe-LIG sheets with 10% nanoparticle concentration showed ∼3 and ∼3.5 times greater charge densities than LIG sheets. The Fe-LIG and SFe-LIG filters showed ∼10 and ∼30% more MB removal compared to LIG under 2.5 V in flow-through mode. Similarly, these filters also showed excellent bacterial and viral inactivation as compared with control LIG filters. Fe-LIG and SFe-LIG filters gave 6-log removal of bacteria under the application of just 2.5 V, which was ∼2-log more removal of bacteria than LIG filters. Regarding virus removal, 6-log removal was obtained at 5 V using Fe-LIG and SFe-LIG filters, which is ∼1.5-log higher than that of LIG filters. The enhanced removal by the Fe-LIG and SFe-LIG surfaces was due to their enhanced charge density, electrochemical activity, and in situ generation of •OH via the electro-Fenton process. Such catalytic LIG surfaces can be applied in various fields for decontamination, electrochemical degradation, microbial inactivation, catalytic electrodes in fuel cells, and ECM filtration for desalination, water, and wastewater treatment. The catalytic Fe-LIG and SFe-LIG filters provide a high flow rate and *in situ* generation of •OH via electro-Fenton in a continuous process. Thus, such Fe-LIG- and SFe-LIG-based filters can be integrated with water and wastewater treatment for enhanced contaminant removal as a continuous process at high flow rates.

https://doi.org/10.1021/acsomega.4c00959
ACS Omega 2024, 9, 22819−22830

■ ASSOCIATED CONTENT

Supporting Information

The Supporting Information is available free of charge at https://pubs.acs.org/doi/10.1021/acsomega.4c00959.

Nanoparticle characterization of nanoparticles with XRD, TEM-EDS mapping, and EDS spectra; EDS elemental composition data for nZVI and S-nZVI; energy-dispersive X-ray spectroscopy of LIG, Fe-LIG, and SFe-LIG sheet; Fe 2p deconvolution of Fe-LIG and SFe-LIG sheets; EDS mapping of SFe-LIG filters; contact angles of LIG filters; FTIR of nanoparticle-incorporated PES membranes and LIG filters; C 1s, O 1s, and S 2p deconvolution for LIG, Fe-LIG, and SFe-LIG filters; Fe 2p deconvolution for Fe-LIG and SFe-LIG filters; cyclic voltagrams and chronoamperogram of LIG, Fe-LIG, and SFe-LIG filters (PDF)

■ AUTHOR INFORMATION

Corresponding Author

Swatantra P. Singh − *Environmental Science and Engineering Department (ESED), Centre for Research in Nanotechnology & Science (CRNTS), Interdisciplinary Program in Climate Studies, and Centre of Excellence on Membrane Technologies for Desalination, Brine Management, and Water Recycling (DeSaltM), Indian Institute of Technology Bombay, Mumbai 400076, India;* orcid.org/0000-0003-1898-3378; Email: swatantra@iitb.ac.in

Authors

Najmul Haque Barbhuiya − *Environmental Science and Engineering Department (ESED), Indian Institute of Technology Bombay, Mumbai 400076, India;* orcid.org/0000-0001-9699-4756

Akhila M. Nair − *Centre for Research in Nanotechnology & Science (CRNTS), Indian Institute of Technology Bombay, Mumbai 400076, India;* orcid.org/0000-0002-9027-6566

Nandini Dixit − *Environmental Science and Engineering Department (ESED), Indian Institute of Technology Bombay, Mumbai 400076, India*

Complete contact information is available at: https://pubs.acs.org/10.1021/acsomega.4c00959

Notes

The authors declare the following competing financial interest(s): NHB has no conflict of interest to declare. Certain aspects of LIG have intellectual property currently owned by the Ben Gurion University of the Negev and IIT Bombay, in which SPS is an inventor and not the officer or director; they granted licenses to a company in return for possible royalties and stock.

■ ACKNOWLEDGMENTS

S.P.S. acknowledges the financial support for this research by the Science and Engineering Research Board (SERB) for CRG grant CRG/2019/005280, the Department of Science & Technology (DST), and the Indian Institute of Technology Bombay (IITB). N.H.B., A.M.N., and N.D. acknowledge the Ministry of Education, India, for their doctoral fellowship support. We appreciate the support provided by the Sophisticated Analytical Instrument Facility (SAIF), Centre Surface Analytical Facility (ESCA), and Metallurgical Engineering and Materials Science Department of IIT Bombay for their analytical facilities.

■ REFERENCES

(1) Comninellis, C.; Kapalka, A.; Malato, S.; Parsons, S. A.; Poulios, I.; Mantzavinos, D. Advanced Oxidation Processes for Water Treatment: Advances and Trends for R&D. *J. Chem. Technol. Biotechnol.* **2008**, *83* (6), 769−776.

(2) Chaplin, B. P. Critical Review of Electrochemical Advanced Oxidation Processes for Water Treatment Applications. *Royal Society of Chemistry* **2014**, *16*, 1182−1203.

(3) Rizzo, L.; Malato, S.; Antakyali, D.; Beretsou, V. G.; Đolić, M. B.; Gernjak, W.; Heath, E.; Ivancev-Tumbas, I.; Karaolia, P.; Lado Ribeiro, A. R.; Mascolo, G.; McArdell, C. S.; Schaar, H.; Silva, A. M. T.; Fatta-Kassinos, D. Consolidated vs New Advanced Treatment Methods for the Removal of Contaminants of Emerging Concern from Urban Wastewater. *Sci. Total Environ.* **2019**, *655*, 986−1008.

(4) Barbhuiya, N. H.; Misra, U.; Singh, S. P. Synthesis, Fabrication, and Mechanism of Action of Electrically Conductive Membranes: A Review. *Environmental Science: Water Research and Technology.* **2021**, *7*, 671−705.

(5) Singla, J.; Thakur, I.; Sangal, V.; Verma, A. Dimensionally Stable Anode (Doped-MMO) Mediated Electro-Oxidation and Multi-Response Optimization Study for Remediation of Urea Wastewater. *Chemosphere* **2021**, *285*, No. 131498.

(6) Karim, A. V.; Nidheesh, P. V.; Oturan, M. A. Boron-Doped Diamond Electrodes for the Mineralization of Organic Pollutants in the Real Wastewater. *Curr. Opin. Electrochem.* **2021**, *30*, No. 100855.

(7) Ken, D. S.; Sinha, A. Dimensionally Stable Anode (Ti/RuO2) Mediated Electro-Oxidation and Multi-Response Optimization Study for Remediation of Coke-Oven Wastewater. *J. Environ. Chem. Eng.* **2021**, *9* (1), No. 105025.

(8) Smith, S. C.; Rodrigues, D. F. Carbon-Based Nanomaterials for Removal of Chemical and Biological Contaminants from Water: A Review of Mechanisms and Applications. *Pergamon* **2015**, *91*, 122−143.

(9) Chakraborty, M.; Hashmi, M. S. J. *Wonder Material Graphene: Properties, Synthesis and Practical Applications.* **2018**, *4* (4), 573−602.

(10) Geim, A. K.; Novoselov, K. S. The Rise of Graphene. *Nat. Mater.* **2007**, *6* (3), 183−191.

(11) Zhao, G.; Wen, T.; Chen, C.; Wang, X. Synthesis of Graphene-Based Nanomaterials and Their Application in Energy-Related and Environmental-Related Areas. *RSC Adv.* **2012**, *2* (25), 9286−9303.

(12) Yin, R.; Guo, W.; Du, J.; Zhou, X.; Zheng, H.; Wu, Q.; Chang, J.; Ren, N. Heteroatoms Doped Graphene for Catalytic Ozonation of Sulfamethoxazole by Metal-Free Catalysis: Performances and Mechanisms. *Chem. Eng. J.* **2017**, *317*, 632−639.

(13) Perreault, F.; Fonseca De Faria, A.; Elimelech, M. Environmental Applications of Graphene-Based Nanomaterials. *Chem. Soc. Rev.* **2015**, *44* (16), 5861−5896.

(14) Nair, A. M.; Kumar, A.; Barbhuiya, N. H.; Singh, S. P. Electrochemical Inactivation of Enteric Viruses MS2, T4, and Phi6 Using Doped Laser-Induced Graphene Electrodes and Filters. *Environ. Sci. Nano* **2023**, *10* (8), 2077−2089.

(15) Kumar, A.; Barbhuiya, N. H.; Jashrapuria, K.; Dixit, N.; Arnusch, C. J.; Singh, S. P. Magnéli-Phase Ti4O7-Doped Laser-Induced Graphene Surfaces and Filters for Pollutant Degradation and Microorganism Removal. *ACS Appl. Mater. Interfaces* **2022**, *14* (46), 52448−52458.

(16) Kumar, A.; Barbhuiya, N. H.; Nair, A. M.; Jashrapuria, K.; Dixit, N.; Singh, S. P. In-Situ Fabrication of Titanium Suboxide-Laser Induced Graphene Composites: Removal of Organic Pollutants and MS2 Bacteriophage. *Chemosphere* **2023**, *335*, No. 138988.

(17) Huang, X.; Yin, Z.; Wu, S.; Qi, X.; He, Q.; Zhang, Q.; Yan, Q.; Boey, F.; Zhang, H. Graphene-Based Materials: Synthesis, Characterization, Properties, and Applications. *Small* **2011**, *7* (14), 1876−1902.

(18) Luong, D. X.; Bets, K. V.; Algozeeb, W. A.; Stanford, M. G.; Kittrell, C.; Chen, W.; Salvatierra, R. V.; Ren, M.; McHugh, E. A.; Advincula, P. A.; Wang, Z.; Bhatt, M.; Guo, H.; Mancevski, V.;

Shahsavari, R.; Yakobson, B. I.; Tour, J. M. Gram-Scale Bottom-up Flash Graphene Synthesis. *Nature* **2020**, *577* (7792), 647−651.
(19) Barbhuiya, N. H.; Kumar, A.; Singh, A.; Chandel, M. K.; Arnusch, C. J.; Tour, J. M.; Singh, S. P. The Future of Flash Graphene for the Sustainable Management of Solid Waste. *ACS Nano* **2021**, *26*, 15461−15470.
(20) Lin, J.; Peng, Z.; Liu, Y.; Ruiz-Zepeda, F.; Ye, R.; Samuel, E. L. G. G.; Yacaman, M. J.; Yakobson, B. I.; Tour, J. M. Laser-Induced Porous Graphene Films from Commercial Polymers. *Nat. Commun.* **2014**, *5* (1), 1−8.
(21) Singh, S. P.; Li, Y.; Zhang, J.; Tour, J. M.; Arnusch, C. J. Sulfur-Doped Laser-Induced Porous Graphene Derived from Polysulfone-Class Polymers and Membranes. *ACS Nano* **2018**, *12* (1), 289−297.
(22) Rathinam, K.; Singh, S. P.; Li, Y.; Kasher, R.; Tour, J. M.; Arnusch, C. J. Polyimide Derived Laser-Induced Graphene as Adsorbent for Cationic and Anionic Dyes. *Carbon N. Y.* **2017**, *124*, 515−524.
(23) Barbhuiya, N. H.; Misra, U.; Singh, S. P. Stacked Laser-Induced Graphene Joule Heaters for Desalination and Water Recycling. *ACS Appl. Nano Mater.* **2022**, *5* (8), 10991−11002.
(24) Dixit, N.; Singh, S. P. Laser-Induced Graphene (LIG) as a Smart and Sustainable Material to Restrain Pandemics and Endemics: A Perspective. *ACS Omega* **2022**, *7* (6), 5112−5130.
(25) Wan, Z.; Umer, M.; Lobino, M.; Thiel, D.; Nguyen, N. T.; Trinchi, A.; Shiddiky, M. J. A.; Gao, Y.; Li, Q. Laser Induced Self-N-Doped Porous Graphene as an Electrochemical Biosensor for Femtomolar MiRNA Detection. *Carbon N. Y.* **2020**, *163*, 385−394.
(26) Peng, Z.; Ye, R.; Mann, J. A.; Zakhidov, D.; Li, Y.; Smalley, P. R.; Lin, J.; Tour, J. M. Flexible Boron-Doped Laser-Induced Graphene Microsupercapacitors. *ACS Nano* **2015**, *9* (6), 5868−5875.
(27) Misra, U.; Dixit, N.; Singh, S. P. Effect of Laser Parameters on Laser-Induced Graphene Filter Fabrication and Its Performance for Desalination and Water Purification. *ACS Appl. Mater. Interfaces* **2023**, *15* (6), 7899−7910.
(28) Li, Y.; Luong, D. X.; Zhang, J.; Tarkunde, Y. R.; Kittrell, C.; Sargunaraj, F.; Ji, Y.; Arnusch, C. J.; Tour, J. M. Laser-Induced Graphene in Controlled Atmospheres: From Superhydrophilic to Superhydrophobic Surfaces. *Adv. Mater.* **2017**, *29* (27), 1700496 DOI: 10.1002/adma.201700496.
(29) Barbhuiya, N. H.; Singh, S. P.; Makovitzki, A.; Narkhede, P.; Oren, Z.; Adar, Y.; Lupu, E.; Cherry, L.; Monash, A.; Arnusch, C. J. Virus Inactivation in Water Using Laser-Induced Graphene Filters. *Materials (Basel).* **2021**, *14* (12), 3179.
(30) Singh, S. P.; Li, Y.; Be'Er, A.; Oren, Y.; Tour, J. M.; Arnusch, C. J. Laser-Induced Graphene Layers and Electrodes Prevents Microbial Fouling and Exerts Antimicrobial Action. *ACS Appl. Mater. Interfaces* **2017**, *9* (21), 18238−18247.
(31) Singh, S. P.; Ramanan, S.; Kaufman, Y.; Arnusch, C. J. Laser-Induced Graphene Biofilm Inhibition: Texture Does Matter. *ACS Appl. Nano Mater.* **2018**, *1* (4), 1713−1720.
(32) Barbhuiya, N. H.; Kumar, A.; Singh, S. P. A Journey of Laser-Induced Graphene in Water Treatment. *Trans. Indian Natl. Acad. Eng.* **2021**, *6* (2), 159−171.
(33) Wang, L.; Wang, Z. Z.; Wang, Z. Z.; Zhang, C.; Wu, Y.; Zheng, H. Enhancement of Antibacterial Function by Incorporation of Silver-Doped ZnO Nanocrystals onto a Laser-Induced Graphene Surface. *RSC Adv.* **2021**, *11* (54), 33883−33889.
(34) Chen, L.; Liao, J.; Zhang, L.; Li, C.; He, S.; Ge, C. Rapid Laser-Induced Highly Dispersed and Ultrafine N-Doped Graphene-Wrapped FeCo2O4 Nanoparticles for Nearly 100% Utilization and Conversion of Peroxymonosulfate into Singlet Oxygen. *ACS EST Water* **2023**, *3*, 542 DOI: 10.1021/acsestwater.2c00563.
(35) Gupta, A.; Holoidovsky, L.; Thamaraiselvan, C.; Thakur, A. K.; Singh, S. P.; Meijler, M. M.; Arnusch, C. J. Silver-Doped Laser-Induced Graphene for Potent Surface Antibacterial Activity and Anti-Biofilm Action. *Chem. Commun.* **2019**, *55* (48), 6890−6893.
(36) Yang, Y.; Li, M.; Zhou, C.; Zhou, K.; Yu, J.; Su, Y.; Hu, N.; Zhang, Y. Laser-Induced MoO x/Sulfur-Doped Graphene Hybrid Frameworks as Efficient Antibacterial Agents. *Langmuir* **2021**, *37* (4), 1596−1604.
(37) Kharisov, B. I.; Rasika Dias, H. V.; Kharissova, O. V.; Manuel Jiménez-Pérez, V.; Olvera Pérez, B.; Muñoz Flores, B. Iron-Containing Nanomaterials: Synthesis, Properties, and Environmental Applications. *RSC Adv.* **2012**, *2* (25), 9325−9358.
(38) Li, S.; Yang, Y.; Zheng, H.; Zheng, Y.; Jing, T.; Ma, J.; Nan, J.; Leong, Y. K.; Chang, J. S. Advanced Oxidation Process Based on Hydroxyl and Sulfate Radicals to Degrade Refractory Organic Pollutants in Landfill Leachate. *Chemosphere* **2022**, *297*, No. 134214.
(39) Yang, S.; Zhang, X.; Tang, J.; Zhang, A. Efficient Degradation of Bisphenol A by the UV-Enhanced Nano Zero-Valent Iron-Activated Hydrogen Peroxide Advanced Oxidation System. *J. Environ. Chem. Eng.* **2022**, *10* (6), No. 108806.
(40) Xu, J.; Li, H.; Lowry, G. V. sulfidized Nanoscale Zero-Valent Iron: Tuning the Properties of This Complex Material for Efficient Groundwater Remediation. *Acc. Mater. Res.* **2021**, *2* (6), 420−431.
(41) Li, J.; Zhang, X.; Sun, Y.; Liang, L.; Pan, B.; Zhang, W.; Guan, X. Advances in sulfidation of Zerovalent Iron for Water Decontamination. *Environ. Sci. Technol.* **2017**, *51* (23), 13533−13544.
(42) Fan, D.; Lan, Y.; Tratnyek, P. G.; Johnson, R. L.; Filip, J.; O'Carroll, D. M.; Nunez Garcia, A.; Agrawal, A. sulfidation of Iron-Based Materials: A Review of Processes and Implications for Water Treatment and Remediation. *Environ. Sci. Technol.* **2017**, *51* (22), 13070−13085.
(43) Jiang, W. L.; Xia, X.; Han, J. L.; Ding, Y. C.; Haider, M. R.; Wang, A. J. Graphene Modified Electro-Fenton Catalytic Membrane for in Situ Degradation of Antibiotic Florfenicol. *Environ. Sci. Technol.* **2018**, *52* (17), 9972−9982.
(44) Liu, M.; Feng, Z.; Luan, X.; Chu, W.; Zhao, H.; Zhao, G. Accelerated Fe2+ Regeneration in an Effective Electro-Fenton Process by Boosting Internal Electron Transfer to a Nitrogen-Conjugated Fe(III) Complex. *Environ. Sci. Technol.* **2021**, *55* (9), 6042−6051.
(45) Chen, Y.; Wang, A.; Zhang, Y.; Bao, R.; Tian, X.; Li, J. Electro-Fenton Degradation of Antibiotic Ciprofloxacin (CIP): Formation of Fe3+-CIP Chelate and Its Effect on Catalytic Behavior of Fe2+/Fe3+ and CIP Mineralization. *Electrochim. Acta* **2017**, *256*, 185−195.
(46) Xu, J.; Avellan, A.; Liu, X.; Lou, Z.; Noël, V.; Lou, Z.; Wang, Y.; Kaegi, R.; Henkelman, G.; Lowry, G. V. Sulfur Loading and Speciation Control the Hydrophobicity, Electron Transfer, Reactivity, and Selectivity of sulfidized Nanoscale Zerovalent Iron. *Adv. Mater.* **2020**, *32* (17), 1906910.
(47) Bhattacharya, M.; Barbhuiya, N. H.; Singh, S. P. Performance Evaluation of Sulfidated Nanoscale Iron for Hexavalent Chromium Removal from Groundwater in Sequential Batch Study. *Environ. Sci. Pollut. Res.* **2023**, *30*, 123055−123066.
(48) Barbhuiya, N. H.; Misra, U.; Kanwar, B.; Singh, S. P. Persulfate Enhanced Ciprofloxacin Removal from Water by Laser-Induced Graphene-Based electroconductive Ultrafiltration Membrane. *Environ. Sci. Water Res. Technol.* **2024**, *10* (2), 442−456.
(49) Halali, M. A.; Larocque, M.; de Lannoy, C. F. Investigating the Stability of Electrically Conductive Membranes. *J. Membr. Sci.* **2021**, *627*, No. 119181.
(50) Halali, M. A.; de Lannoy, C. F. Methods for Stability Assessment of Electrically Conductive Membranes. *MethodsX* **2022**, *9*, No. 101627.
(51) Kosaka, K.; Yamada, H.; Matsui, S.; Echigo, S.; Shishida, K. Comparison among the Methods for Hydrogen Peroxide Measurements to Evaluate Advanced Oxidation Processes: Application of a Spectrophotometric Method Using Copper(II) Ion and 2,9-Dimethyl-1,10-Phenanthroline. *Environ. Sci. Technol.* **1998**, *32* (23), 3821−3824.
(52) Posada, J. O. G.; Hall, P. J. Controlling Hydrogen Evolution on Iron Electrodes. *Int. J. Hydrogen Energy* **2016**, *41* (45), 20807−20817.
(53) Santos, N. F.; Rodrigues, J.; Pereira, S. O.; Fernandes, A. J. S.; Monteiro, T.; Costa, F. M. Electrochemical and Photoluminescence Response of Laser-Induced Graphene/Electrodeposited ZnO Composites. *Sci. Reports 2021 111* **2021**, *11* (1), 1−15.

https://doi.org/10.1021/acsomega.4c00959
ACS Omega 2024, 9, 22819−22830

(54) Ghosh, D.; Giri, S.; Moniruzzaman, M.; Basu, T.; Mandal, M.; Das, C. K. α MnMoO4/Graphene Hybrid Composite: High Energy Density Supercapacitor Electrode Material. *Dalt. Trans.* **2014**, *43* (28), 11067−11076.
(55) Yu, L.; Akolkar, R. Lead Underpotential Deposition for the Surface Characterization of Silver Ad-Atom Modified Gold Electrocatalysts for Glucose Oxidation. *J. Electroanal. Chem.* **2017**, *792*, 61−65.
(56) Dreyfus, R. W. CN Temperatures above Laser Ablated Polyimide. *Appl. Phys. A 1992 554* **1992**, *55* (4), 335−339.
(57) Malard, L. M.; Pimenta, M. A.; Dresselhaus, G.; Dresselhaus, M. S. Raman Spectroscopy in Graphene. *Phys. Rep.* **2009**, *473* (5−6), 51−87.
(58) Poh, H. L.; Šimek, P.; Sofer, Z.; Pumera, M. Sulfur-Doped Graphene via Thermal Exfoliation of Graphite Oxide in H2S, SO2, or CS2 Gas. *ACS Nano* **2013**, *7* (6), 5262−5272.
(59) Ren, M.; Zhang, J.; Tour, J. M. Laser-Induced Graphene Synthesis of Co3O4 in Graphene for Oxygen Electrocatalysis and Metal-Air Batteries. *Carbon N. Y.* **2018**, *139*, 880−887.
(60) Han, Y.; Ghoshal, S.; Lowry, G. V.; Chen, J. A Comparison of the Effects of Natural Organic Matter on Sulfidated and Non-sulfidated Nanoscale Zerovalent Iron Colloidal Stability, Toxicity, and Reactivity to Trichloroethylene. *Sci. Total Environ.* **2019**, *671*, 254−261.
(61) Mullet, M.; Boursiquot, S.; Abdelmoula, M.; Génin, J. M.; Ehrhardt, J. J. Surface Chemistry and Structural Properties of Mackinawite Prepared by Reaction of Sulfide Ions with Metallic Iron. *Geochim. Cosmochim. Acta* **2002**, *66* (5), 829−836.
(62) Zhang, D.; Li, Y.; Tong, S.; Jiang, X.; Wang, L.; Sun, X.; Li, J.; Liu, X.; Shen, J. Biochar Supported Sulfide-Modified Nanoscale Zero-Valent Iron for the Reduction of Nitrobenzene. *RSC Adv.* **2018**, *8* (39), 22161−22168.
(63) Wang, C.; Yao, D.; Liu, Y.; Wu, Y.; Shen, J. Development of a Novel Recycling System for Waste Cathode Ray Tube Funnel Glass Based on the Integration of Nanoscale Fe0 with Ball Milling. *Waste Manag.* **2018**, *76*, 679−686.
(64) Li, L.; Ma, P.; Hussain, S.; Jia, L.; Lin, D.; Yin, X.; Lin, Y.; Cheng, Z.; Wang, L. FeS2/Carbon Hybrids on Carbon Cloth: A Highly Efficient and Stable Counter Electrode for Dye-Sensitized Solar Cells. *Sustain. Energy Fuels* **2019**, *3* (7), 1749−1756.
(65) Xu, J.; Wang, Y.; Weng, C.; Bai, W.; Jiao, Y.; Kaegi, R.; Lowry, G. V. Reactivity, Selectivity, and Long-Term Performance of sulfidized Nanoscale Zerovalent Iron with Different Properties. *Environ. Sci. Technol.* **2019**, *53* (10), 5936−5945.
(66) Zhang, Y.; Duan, Z.; Jin, Y.; Han, H.; Xu, C. Chemical Bond Bridging across Two Domains: Generation of Fe(II) and In Situ Formation of FeSx on Zerovalent Iron. *Environ. Sci. Technol.* **2023**, *57*, 11336 DOI: 10.1021/acs.est.3c02768.
(67) Zhang, C.; Deng, L.; Zhang, P.; Ren, X.; Li, Y.; He, T. Electrospun FeS Nanorods with Enhanced Stability as Counter Electrodes for Dye-Sensitized Solar Cells. *Electrochim. Acta* **2017**, *229*, 229−238.
(68) Thakur, A. K.; Singh, S. P.; Kleinberg, M. N.; Gupta, A.; Arnusch, C. J. Laser-Induced Graphene-PVA Composites as Robust Electrically Conductive Water Treatment Membranes. *ACS Appl. Mater. Interfaces* **2019**, *11* (11), 10914−10921.
(69) Duan, W.; Ronen, A.; Walker, S.; Jassby, D. Polyaniline-Coated Carbon Nanotube Ultrafiltration Membranes: Enhanced Anodic Stability for in Situ Cleaning and Electro-Oxidation Processes. *ACS Appl. Mater. Interfaces* **2016**, *8* (34), 22574−22584.
(70) Zhu, X.; Le, T. T.; Du, J.; Xu, T.; Cui, Y.; Ling, H.; Kim, S. H. Novel Core-Shell Sulfidated Nano-Fe(0) Particles for Chromate Sequestration: Promoted Electron Transfer and Fe(II) Production. *Chemosphere* **2021**, *284*, No. 131379.
(71) Kumar, A.; Barbhuiya, N. H.; Singh, S. P. Magnéli phase titanium sub-oxides synthesis, fabrication and its application for environmental remediation: Current status and prospect. *Chemosphere* **2022**, *307*, No. 135878.
(72) Wang, W.; Lu, Y.; Luo, H.; Liu, G.; Zhang, R.; Jin, S. A Microbial Electro-Fenton Cell for Removing Carbamazepine in Wastewater with Electricity Output. *Water Res.* **2018**, *139*, 58−65.
(73) Gupta, A.; Sharma, C. P.; Thamaraiselvan, C.; Pisharody, L.; Powell, C. D.; Arnusch, C. J. Low-Voltage Bacterial and Viral Killing Using Laser-Induced Graphene-Coated Non-Woven Air Filters. *ACS Appl. Mater. Interfaces* **2021**, *13* (49), 59373−59380.
(74) Huang, L.; Cheng, L.; Ma, T.; Zhang, J.-J.; Wu, H.; Su, J.; Song, Y.; Zhu, H.; Liu, Q.; Zhu, M.; Zeng, Z.; He, Q.; Tse, M.-K.; Yang, D.-t; Yakobson, B. I.; Tang, B. Z.; Ren, Y.; Ye, R. Direct Synthesis of Ammonia from Nitrate on Amorphous Graphene with Near 100% Efficiency. *Adv. Mater.* **2023**, *35* (24), 2211856.
(75) Cheng, L.; Ma, T.; Zhang, B.; Huang, L.; Guo, W.; Hu, F.; Zhu, H.; Wang, Z.; Zheng, T.; Yang, D.-T.; Siu, C.-K.; Liu, Q.; Ren, Y.; Xia, C.; Tang, B. Z.; Ye, R. Steering the Topological Defects in Amorphous Laser-Induced Graphene for Direct Nitrate-to-Ammonia Electroreduction. *ACS Catal.* **2022**, *12* (19), 11639−11650.
(76) Xu, M.; Wu, C.; Zhou, Y.; Xu, M.; Wu, C.; Zhou, Y. Advancements in the Fenton Process for Wastewater Treatment. *Adv. Oxid. Process* **2020**, *61*, 61 DOI: 10.5772/INTECHOPEN.90256.
(77) Kishimoto, N.; Kitamura, T.; Kato, M.; Otsu, H. Reusability of Iron Sludge as an Iron Source for the Electrochemical Fenton-Type Process Using Fe2+/HOCl System. *Water Res.* **2013**, *47* (5), 1919−1927.

https://doi.org/10.1021/acsomega.4c00959
ACS Omega 2024, 9, 22819−22830